Notable Effect of the Subgrid-scale Stress Anisotropy on Mean-Velocity Prediction through Budget of the Grid-scale Reynolds-Shear Stress

ABE, Ken-ichi
Department of Aeronautics and Astronautics, Faculty of Engineering, Kyushu University : Professor

出版情報：Physics of Fluids. 31 (10), pp.105103-, 2019-10. AIP Publishing
バージョン：

Physics of Fluids

Notable effect of the subgrid-scale stress anisotropy on mean-velocity prediction through budget of the grid-scale Reynolds-shear stress

Cite as: Phys. Fluids **31**, 105103 (2019); https://doi.org/10.1063/1.5121528
Submitted: 26 July 2019 . Accepted: 20 September 2019 . Published Online: 08 October 2019

Ken-ichi Abe

Notable effect of the subgrid-scale stress anisotropy on mean-velocity prediction through budget of the grid-scale Reynolds-shear stress

Cite as: Phys. Fluids 31, 105103 (2019); doi: 10.1063/1.5121528
Submitted: 26 July 2019 • Accepted: 20 September 2019 •
Published Online: 8 October 2019

Ken-ichi Abe[a)]

AFFILIATIONS

Department of Aeronautics and Astronautics, Kyushu University, 744, Motooka, Nishi-ku, Fukuoka 819-0395, Japan

[a)]Electronic mail: abe@aero.kyushu-u.ac.jp

ABSTRACT

In large eddy simulation (LES), the mean-velocity distribution in wall turbulence depends strongly on the distribution of the ensemble-averaged Reynolds (*Re*) shear stress, which consists of two parts: the resolved grid-scale (GS) and unresolved subgrid-scale (SGS) components. As the grid resolution becomes coarser, the GS component decreases and thus the SGS component must increase to compensate for this. The GS decrease is originally caused by filtering, through which the power spectrum is cut off mainly in the high-wavenumber region. Therefore, the SGS model has been discussed mostly in terms of the energy transfer between the GS and SGS components. Recently, however, some studies have found that the SGS-stress anisotropy directly influences instantaneous GS vortex motions. This also means that the SGS stress may have a large effect on the ensemble-averaged GS *Re* stress because the instantaneous fluctuation of the SGS stress correlates with that of the velocity gradient in the GS budget. In this study, we investigate in detail the effect of the SGS stress on predicting the resolved GS *Re* shear stress through its budget. For this purpose, we perform *a priori* tests with highly resolved LES data of a plane channel flow. The knowledge obtained is then confirmed by *a posteriori* tests for various grid resolutions and Reynolds numbers. It is found that the SGS-stress anisotropy is very important for providing a reasonable trend of the GS *Re* shear stress, leading to more accurate prediction of the mean velocity for coarse-grid resolutions.

I. INTRODUCTION

Large eddy simulation (LES) has long been used to predict complex turbulence in engineering applications. In LES, a flow variable is decomposed into a directly resolved grid-scale (GS) component and an unresolved subgrid-scale (SGS) component.

The canonical governing equations for incompressible turbulence may be written as

$$\frac{\partial \overline{U}_i}{\partial t} + \frac{\partial \overline{U}_i \overline{U}_j}{\partial x_j} = -\frac{1}{\rho}\frac{\partial \overline{P}}{\partial x_i} + \frac{\partial}{\partial x_j}\left(2\nu S_{ij} - {\tau_{ij}}^a\right), \qquad \frac{\partial \overline{U}_i}{\partial x_i} = 0, \quad S_{ij} = \frac{1}{2}\left(\frac{\partial \overline{U}_i}{\partial x_j} + \frac{\partial \overline{U}_j}{\partial x_i}\right), \tag{1}$$

where $\overline{(\ )}$ denotes a filtered value. The quantities ρ, $\overline{P}$, $\overline{U}_i$, ν, and S_{ij} are the density, filtered static pressure, filtered velocity, kinematic viscosity, and strain-rate tensor, respectively. Note that ${\tau_{ij}}^a$ is defined as ${\tau_{ij}}^a = \tau_{ij} - \tau_{kk}\delta_{ij}/3$, where the SGS stress τ_{ij} is originally expressed as

$$\tau_{ij} = \overline{U_i U_j} - \overline{U}_i \overline{U}_j. \tag{2}$$

Therefore, $\overline{P}$ in Eq. (1) includes $\rho\tau_{kk}/3$ in this study.

Because LES success requires accurate representation of the SGS stress, a number of research groups[1–15] have proposed several SGS models for τ_{ij}. Although these models have provided encouraging results, there remain several aspects to be further improved. Among them, an important concern is the reduction of the predictive accuracy when an SGS model is applied to an engineering application using a coarse-grid resolution, particularly near the wall.

Generally, a conventional linear eddy-viscosity model (EVM) such as the Smagorinsky model[1] (SM) does not show the correct principal direction of the real SGS stress. A dynamic Smagorinsky

model (DSM) promises better performance (Refs. 2 and 3). However, the correct principal direction cannot be reproduced within the framework of an EVM, although this model potentially provides both the forward and backward scatters. This type of SGS model is also known to cause numerical instability, owing to the effect of this backward scatter.

Another approach, referred to as "implicit LES," has shown promise for practical LES. In general, this method does not explicitly introduce any SGS model. Instead of an SGS model, the dissipative feature originally involved in the discretization scheme is expected to suffice for properly extracting the kinetic energy from the GS component. Although the implicit LES is becoming increasingly popular in this research field,[4–7] its performance depends strongly on the dissipative feature originating from the discretization scheme. Because this strategy focuses mainly on energy transfer, it does not always account for the detailed dynamics of small-scale turbulent structures. Therefore, it is difficult to discuss how each implicit LES deals with the SGS-stress components in the calculation process.

An alternative method for a physics-oriented improvement of the predictive accuracy is the scale-similarity model, the most popular version of which is the model proposed by Bardina *et al.*[8] This type of model provides much better alignment with the real SGS stress tensor.[9] However, it is not always dissipative and often suffers from numerical instability. The concept of a mixed model[10–15] is worth noting as a remedy. The mixed model is a combination of the scale-similarity model and a dissipative EVM such as the SM. Although mixed SGS models provide encouraging results, their computational stability for complex turbulence is still unknown because the scale-similarity model originally involves some backward-scattering effect. In fact, they have not been applied much to practical engineering problems with complex geometries.

To overcome this difficulty, Abe[16] recently proposed a new anisotropy-resolving SGS model, where the SGS-stress expression is constructed by combining an isotropic EVM with an extra anisotropic term (EAT) that excludes a possible numerical instability from a scale-similarity model. This SGS model successfully improved predictive accuracy, particularly with a coarse grid near the wall, while maintaining computational stability. Although this modeling concept has been successfully applied to several test cases,[16,17] it is not yet clear how the anisotropic term works for improving the predictive performance.

In LES, the mean-velocity distribution in wall turbulence depends strongly on the distribution of the ensemble-averaged Reynolds (*Re*) shear stress, which consists of both the GS and SGS components. Generally, as the grid resolution becomes coarser, the GS component decreases and thus the SGS component must increase to compensate for the GS component. The GS decrease is originally caused by filtering, through which the power spectrum is considered to be cut off mainly in the high-wavenumber region. Therefore, the SGS model has been discussed mostly in terms of the energy transfer between the GS and SGS components. Our recent studies,[18,19] however, have found that an anisotropic SGS model effectively enhances near-wall turbulent vortexes. This also means that an SGS model may directly affect statistical values of the GS flow field.

Considering Eq. (1) being ensemble-averaged, we obtain the equation

$$\frac{\partial\langle\overline{U}_i\rangle}{\partial t}+\frac{\partial\langle\overline{U}_i\rangle\langle\overline{U}_j\rangle}{\partial x_j}=-\frac{1}{\rho}\frac{\partial\langle\overline{P}\rangle}{\partial x_i}+\frac{\partial}{\partial x_j}\left(2\nu\langle S_{ij}\rangle-\langle\tau_{ij}{}^{a}\rangle-\langle u_i''u_j''\rangle\right), \tag{3}$$

where $\langle\ \rangle$ denotes an ensemble-averaged quantity, a double prime means its fluctuation (i.e., $u_i''=\overline{U}_i-\langle\overline{U}_i\rangle$), and $\langle u_i''u_j''\rangle$ is the resolved GS *Re* stress. To study the GS behavior in more detail, we consider the budget of $\langle u_i''u_j''\rangle$.

From Eqs. (1) and (3), we obtain the transport equation of u_i'', and then, the transport equation of $\langle u_i''u_j''\rangle$ is obtained as follows:

$$\frac{\partial\langle u_i''u_j''\rangle}{\partial t}+\langle\overline{U}_k\rangle\frac{\partial\langle u_i''u_j''\rangle}{\partial x_k}=P_{ij}-\varepsilon_{ij}+\phi_{ij}+\xi_{ij}+\frac{\partial}{\partial x_k}\left(D_{ijk}+T_{ijk}+J_{ijk}+\zeta_{ijk}\right), \tag{4}$$

where

$$\begin{gathered}P_{ij}=-\langle u_i''u_k''\rangle\frac{\partial\langle\overline{U}_j\rangle}{\partial x_k}-\langle u_j''u_k''\rangle\frac{\partial\langle\overline{U}_i\rangle}{\partial x_k},\quad D_{ijk}=\nu\frac{\partial\langle u_i''u_j''\rangle}{\partial x_k},\\ \phi_{ij}=\left\langle\frac{p''}{\rho}\left(\frac{\partial u_i''}{\partial x_j}+\frac{\partial u_j''}{\partial x_i}\right)\right\rangle,\quad \xi_{ij}=\left\langle\tau_{ik}{}^{a''}\frac{\partial u_j''}{\partial x_k}+\tau_{jk}{}^{a''}\frac{\partial u_i''}{\partial x_k}\right\rangle,\\ \varepsilon_{ij}=2\nu\left\langle\frac{\partial u_i''}{\partial x_k}\frac{\partial u_j''}{\partial x_k}\right\rangle,\quad \zeta_{ijk}=-\left(\left\langle\tau_{ik}{}^{a''}u_j''\right\rangle+\left\langle\tau_{jk}{}^{a''}u_i''\right\rangle\right),\\ T_{ijk}=-\langle u_i''u_j''u_k''\rangle,\quad J_{ijk}=-\left(\langle p''u_i''\rangle\delta_{jk}+\langle p''u_j''\rangle\delta_{ik}\right).\end{gathered} \tag{5}$$

In Eq. (5), $\tau_{ij}{}^{a''}$ is the instantaneous fluctuation of $\tau_{ij}{}^{a}$ defined as $\tau_{ij}{}^{a''}=\tau_{ij}{}^{a}-\langle\tau_{ij}{}^{a}\rangle$. All terms except for ξ_{ij} and ζ_{ijk} on the right side of Eq. (4) have the same definitions as generally known. Therefore, the two terms ξ_{ij} and ζ_{ijk} are newly added in the budget of the GS *Re* stress in LES. Hereafter, we call ξ_{ij} the "SGS-strain term" and ζ_{ijk} the "SGS diffusion term." It is clear that the instantaneous fluctuations u_i'' and $\tau_{ij}{}^{a''}$ are closely coupled in these terms, and thus, not only $\langle\tau_{ij}{}^{a}\rangle$ in Eq. (3) but also its fluctuation $\tau_{ij}{}^{a''}$ are very important for accurately predicting the mean velocity through the $\langle u_i''u_j''\rangle$ budget.

Thus, in this study, we investigate in detail the effect of the SGS stress on predicting the resolved GS *Re* stress through its budget. Primary attention is paid to the budget of the GS *Re* shear stress $\langle u''v''\rangle$, which is most important for predicting the streamwise mean velocity $\langle\overline{U}\rangle$ in a wall-shear flow. We perform *a priori* tests using highly resolved LES data of a fully developed plane channel flow. By filtering the LES data, all terms in the $\langle u''v''\rangle$ budget are calculated for various coarse grid resolutions. We then compare the predictions of conventional EVM-type SGS models and an anisotropy-resolving SGS model with the filtered data. Furthermore, the knowledge obtained is confirmed by *a posteriori* tests for various grid resolutions and Reynolds numbers.

II. FLOW DATA USED FOR DETAILED INVESTIGATIONS

A. Test cases and computational conditions

In this study, we investigate the LES results for a plane channel flow that were originally obtained by Abe.[20] The computational

TABLE I. Computational parameters for channel flow. The computational domain is fixed to $6.4\delta \times 2\delta \times 3.2\delta$ for all test cases.

Case	Re_τ	Model	Grid type	Grid numbers	Δx	Δy	Δz	Δx^+	Δy^+	Δz^+	Δt
C395A	395	SMM[16]	Finest	$513 \times 98 \times 513$	0.0125	$1 \times 10^{-3} - 0.05$	0.006 25	5	0.4–20	2.5	3×10^{-4}
C395B	395	SMM	Fine	$257 \times 98 \times 257$	0.025	$1 \times 10^{-3} - 0.05$	0.012 5	10	0.4–20	5	3×10^{-4}
C395C	395	SMM	Medium	$129 \times 98 \times 129$	0.05	$1 \times 10^{-3} - 0.05$	0.025	20	0.4–20	10	5×10^{-4}
C395D	395	SMM	Coarse	$65 \times 98 \times 65$	0.1	$1 \times 10^{-3} - 0.05$	0.05	40	0.4–20	20	1×10^{-3}
C395E	395	SMM	Coarsest	$33 \times 98 \times 33$	0.2	$1 \times 10^{-3} - 0.05$	0.1	80	0.4–20	40	1×10^{-3}
C395F	395	EVM	Fine	$257 \times 98 \times 257$	0.025	$1 \times 10^{-3} - 0.05$	0.012 5	10	0.4–20	5	3×10^{-4}
C395G	395	EVM	Medium	$129 \times 98 \times 129$	0.05	$1 \times 10^{-3} - 0.05$	0.025	20	0.4–20	10	5×10^{-4}
C395H	395	EVM	Coarse	$65 \times 98 \times 65$	0.1	$1 \times 10^{-3} - 0.05$	0.05	40	0.4–20	20	1×10^{-3}
C395I	395	EVM	Coarsest	$33 \times 98 \times 33$	0.2	$1 \times 10^{-3} - 0.05$	0.1	80	0.4–20	40	1×10^{-3}
C1E3J	1000	SMM	...	$65 \times 181 \times 65$	0.1	$3 \times 10^{-4} - 0.03$	0.05	100	0.3–30	50	3×10^{-4}
C1E3K	1000	EVM	...	$65 \times 181 \times 65$	0.1	$3 \times 10^{-4} - 0.03$	0.05	100	0.3–30	50	3×10^{-4}
C2E3L	2000	SMM	...	$129 \times 181 \times 129$	0.05	$3 \times 10^{-4} - 0.03$	0.025	100	0.6–60	50	2×10^{-4}
C2E3M	2000	EVM	...	$129 \times 181 \times 129$	0.05	$3 \times 10^{-4} - 0.03$	0.025	100	0.6–60	50	2×10^{-4}
C395O	395	No SGS model	Fine	$257 \times 98 \times 257$	0.025	$1 \times 10^{-3} - 0.05$	0.012 5	10	0.4–20	5	3×10^{-4}
C395P	395	No SGS model	Medium	$129 \times 98 \times 129$	0.05	$1 \times 10^{-3} - 0.05$	0.025	20	0.4–20	10	5×10^{-4}
C395Q	395	No SGS model	Coarse	$65 \times 98 \times 65$	0.1	$1 \times 10^{-3} - 0.05$	0.05	40	0.4–20	20	1×10^{-3}
C395R	395	No SGS model	Coarsest	$33 \times 98 \times 33$	0.2	$1 \times 10^{-3} - 0.05$	0.1	80	0.4–20	40	1×10^{-3}

parameters are listed in Table I, where $(\,)_+$ denotes a quantity in the wall unit. In the table, the symbol "SMM" means an anisotropy-resolving SGS model by Abe[16] that is named the "stabilized mixed model" (SMM hereafter), while "EVM" denotes its isotropic version. Note that brief descriptions of these SGS models including the origin of the name "SMM" will be given in Sec. III.

The Reynolds number Re_τ for the basic test cases in Table I was 395, which corresponds to the direct numerical simulation (DNS) of Moser *et al.*[21] ($Re_\tau = u_\tau\delta/\nu$, where u_τ is the friction velocity and δ is the half-channel height). Note that in addition to the test cases in the work of Abe,[20] we added other cases with a much coarser grid resolution ($\Delta x^+ = 80$, $\Delta z^+ = 40$; referred to as the "coarsest" grid). Furthermore, to make the role of the anisotropic term clearer, calculations with no SGS model were performed using the same grid resolutions as C395B, C395C, C395D, and C395E. We also performed calculations at much higher Reynolds numbers ($Re_\tau = 1000$, 2000) with a coarse grid resolution ($\Delta x^+ = 100$, $\Delta z^+ = 50$) similar to that of the aforementioned coarsest grid in Table I. The obtained results are compared with the corresponding DNS data by Lee and Moser.[22] The cases of higher Re are expected to provide useful knowledge on the model performance when applied to more practical high Re turbulent flows.

The computational domain was fixed to $6.4\delta \times 2\delta \times 3.2\delta$ in the streamwise (x), wall-normal (y), and spanwise (z) directions, respectively. As seen in Table I, we tested five types of grid nodes for simulations at $Re_\tau = 395$, among which the finest grid, $513 \times 98 \times 513$ (C395A), was expected to provide highly resolved results with quality sufficiently close to that of the DNS. Therefore, we treat the C395A results as the true values for reference in the following discussion. Other computational procedures including the boundary conditions and numerical schemes are described in the work of Abe.[16]

B. Fundamental features of simulation results

First, to confirm the basic performance of the SGS models adopted, we compare the mean-velocity distributions for $Re_\tau = 395$ with various grid resolutions in Fig. 1. In the figure, panels (a) and (b) are the SMM and EVM results, respectively, and (c) shows the results with no SGS model. Note that the results for C395A are also included in Fig. 1(b) for reference.

For a more detailed discussion, the error in the prediction of the skin friction coefficient C_f is investigated. The error in C_f is defined as

$$\text{Error (\%)} = \frac{C_f - C_{f,DNS}}{C_{f,DNS}} \times 100, \quad C_f = \frac{\tau_w}{\rho U_b{}^2/2}, \tag{6}$$

where τ_w and U_b denote the mean wall-shear stress and the bulk-mean velocity, respectively. The predicted C_f is compared with the DNS data in Table II. Note that the bulk-mean velocity in the wall unit U_b^+ is also compared in the table.

The SMM results in Fig. 1(a) agree well with those of the DNS[21] regardless of grid resolution. This can also be confirmed quantitatively from the data in Table II. In contrast, the EVM performance in Fig. 1(b) worsens as the grid resolution becomes coarser, particularly for C395H and C395I. This decline in predictive accuracy typically occurs in conventional isotropic SGS models.

On the other hand, it is a little surprising that the predictions obtained with no SGS model are rather reasonable for fine- and medium-grid resolutions compared with those from the EVM. Even for C395Q with a coarse grid resolution, the prediction accuracy is still sufficiently high. In general, a calculation using the spectral method with an insufficient grid resolution often shows a downward shift in the mean-velocity distribution compared with the DNS

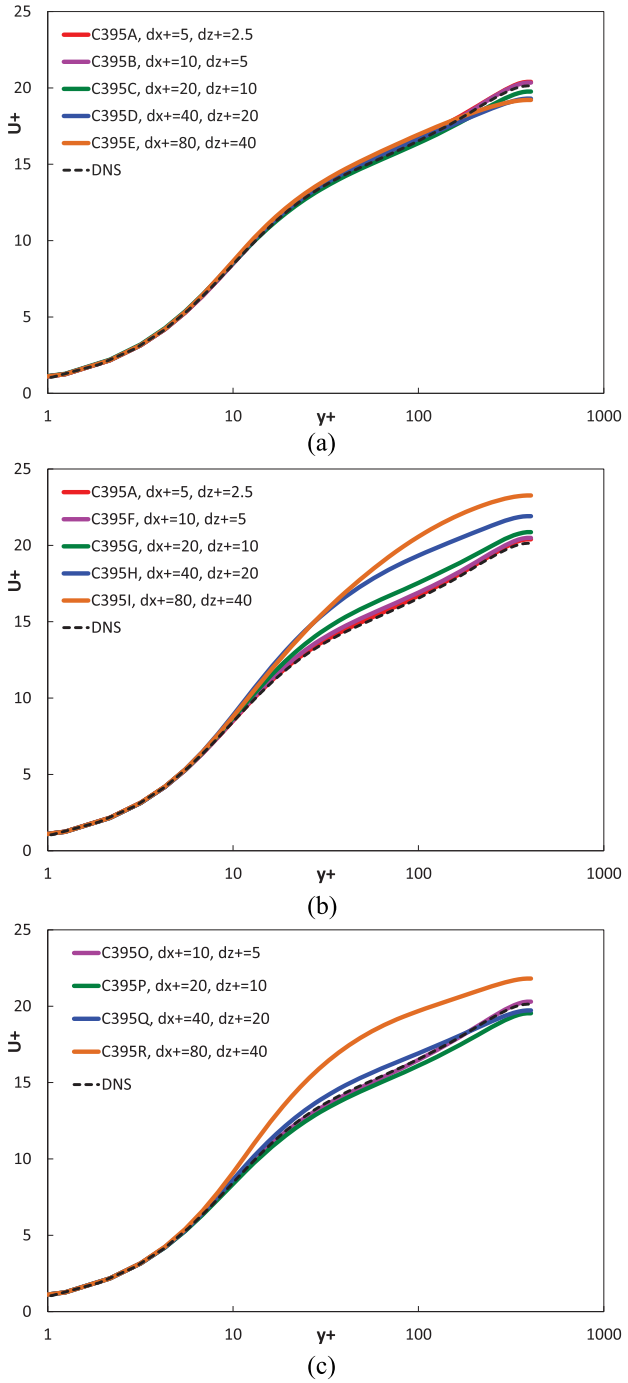

FIG. 1. Mean-velocity predictions for various grid resolutions: (a) SMM, (b) EVM, (c) no SGS model. The finest-grid case (C395A) is included in (b) for reference.

data.[15] In contrast, the present calculation adopts the second-order central difference scheme,[16,20] making the computational results dissipative compared with the spectral method. Because these two factors work in opposite directions, it sometimes results in a reasonable

TABLE II. Comparison of the bulk-mean velocity U_b^+ and the friction coefficient C_f with the DNS data[21] for Re_τ = 395.

Case	Model	U_b^+	Error (%)	C_f	Error (%)
DNS[21]		17.55		6.50×10^{-3}	
C395A	SMM	17.70	0.90	6.38×10^{-3}	−1.78
C395B	SMM	17.61	0.37	6.45×10^{-3}	−0.73
C395C	SMM	17.58	0.21	6.47×10^{-3}	−0.42
C395D	SMM	17.24	−1.76	6.73×10^{-3}	3.61
C395E	SMM	17.37	−0.97	6.63×10^{-3}	1.97
C395F	EVM	17.89	1.99	6.25×10^{-3}	−3.86
C395G	EVM	18.15	3.47	6.07×10^{-3}	−6.6
C395H	EVM	19.70	12.31	5.15×10^{-3}	−20.72
C395I	EVM	21.13	20.44	4.48×10^{-3}	−31.07
C395O	No SGS model	17.58	0.22	6.47×10^{-3}	−0.44
C395P	No SGS model	17.06	−2.78	6.87×10^{-3}	5.80
C395Q	No SGS model	17.56	0.09	6.49×10^{-3}	−0.18
C395R	No SGS model	19.86	13.17	5.07×10^{-3}	−21.92

prediction of the mean velocity. This situation can be considered as an implicit LES. However, for C395R with the coarsest grid resolution, the prediction accuracy with no SGS model rapidly worsens. This is because the grid resolution is close to (or a little larger than) the representative scale of turbulent vortex structures in the near-wall region; thus, these structures cannot be properly captured by the discretization scheme used in this study.

In contrast, the SMM provides reasonable predictions even under such a severe condition of C395E, as seen in Fig. 1(a) and Table II. This is a notable feature of the present anisotropic SGS model. Our previous studies[18,19] indicated that the SMM enhanced near-wall vortex structures for coarser grid resolutions. This fact is considered to be closely related to the improvement of the prediction accuracy.

In general, LES depends strongly on the numerical scheme as well as the SGS model adopted in each program code. There are a number of combinations of the discretization scheme, SGS model, and grid topology.[23] Calculations with no SGS model may provide reasonable results as an implicit LES for moderate grid resolutions. In such cases, introduction of an isotropic SGS model is likely to make the results more dissipative, leading to worse predictions. However, the performance of such an implicit LES may rapidly worsen as the grid resolution becomes close to the scale of representative vortex structures. Such a rapid decline in predictive accuracy is undesirable for practical LES because engineering applications may include a wide range of grid resolutions.

An important feature of the anisotropic term in the SMM is that it yields strictly no energy transfer between the GS and SGS components.[16,17] This is the reason why the SMM provides more stable computation compared with conventional scale-similarity models. Considering the remarkable improvement of the prediction accuracy for the coarsest grid (C395E) without any energy transfer by the EAT, an important role of an SGS model is to directly enhance GS structures through the momentum equation in Eq. (1). In this sense, a detailed investigation of the budget of the GS *Re* shear stress

is very important for further development of practical LES including coarse grid resolutions.

Figure 2 shows the *Re* shear stress predicted by the SMM. The aforementioned feature in the mean-velocity predictions is reasonably explained from Fig. 2(a), where the total (GS + SGS) values predicted by the SMM show almost no grid dependency. However, the balance between the GS and SGS parts changes according to grid resolution. As the grid resolution becomes coarser, the GS part decreases and the SGS part increases. Note that Fig. 2(c) confirms again that the SGS model has almost no effect in C395A.

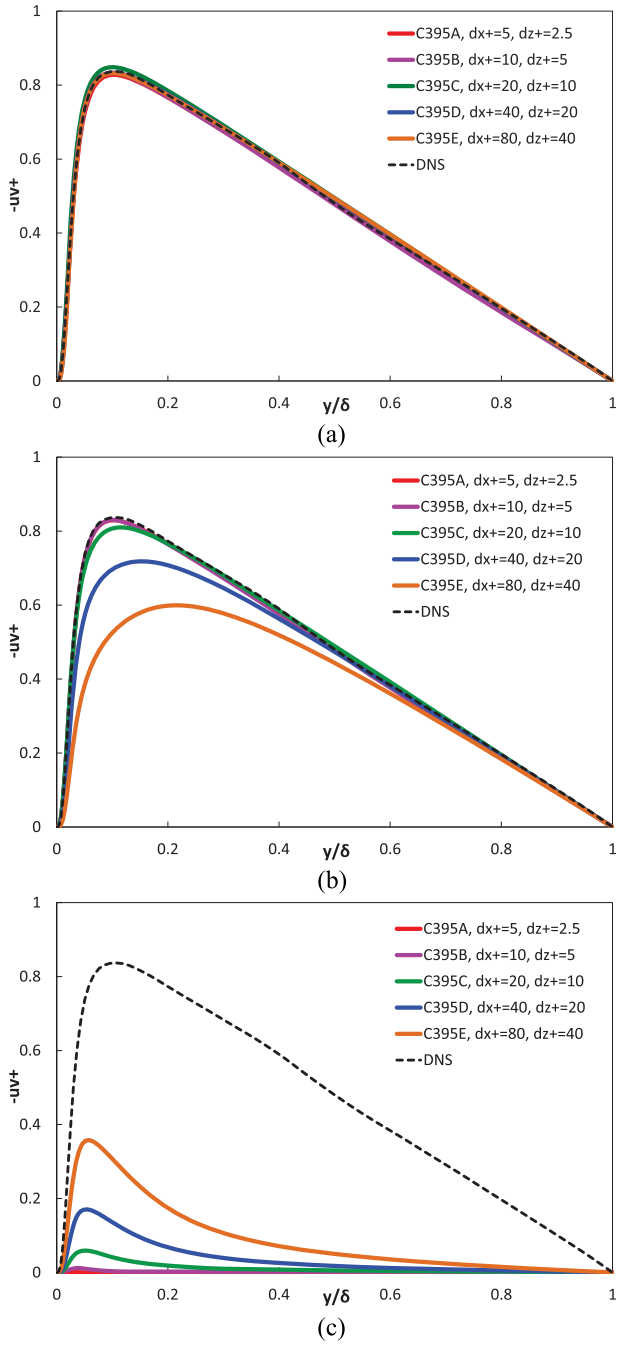

FIG. 2. Total (GS + SGS), GS, and SGS *Re* shear stress for various grid resolutions calculated by SMM: (a) Total (GS + SGS) *Re* shear stress, (b) resolved GS part, $\langle u''v'' \rangle$, and (c) modeled SGS part, $\langle \tau_{12} \rangle$.

Researchers have thought that the primary role of the SGS part is to compensate for the decrease in the GS part according to the grid resolution, as seen in Fig. 2(c). However, our previous studies[18,19] found that the anisotropic part of the SMM directly enhanced turbulent vortex structures. This also means that the GS component is strongly affected by an SGS model. Therefore, an aim of this study is to reveal how an SGS model directly affects prediction of the ensemble-averaged GS *Re* stress in Fig. 2(b).

To understand the scale distribution of turbulence in the calculated flows, we compare the energy spectra of the streamwise velocity at $y^+ = 20$ for various grid resolutions. Figures 3(a) and 3(b) show the energy spectra obtained from the simulation results by the SMM and EVM, respectively, while Figs. 3(c) and 3(d) show those of the GS and SGS components, respectively, obtained from the finest-grid data (C395A) using the top-hat filter. Note that the original energy spectrum for C395A (red line) is also included in all panels of Fig. 3 for reference.

The SMM results in Fig. 3(a) show a trend similar to that of the filtered values obtained from the finest-grid data in Fig. 3(c), while the EVM energy spectra decay more rapidly for coarse grids. Treating the finest-grid results as the true values, we consider the spectra in Fig. 3(c) calculated with the top-hat filter to be ideal distributions. The SMM thus performs much better than the EVM, particularly for coarse grids. We expect that the SMM has a capability of providing reasonable energy spectra in wavenumber regions close to the filter width used.

Another notable feature of Fig. 3(d) is that the SGS component is significant even in the low-wavenumber region. It is generally known that the SGS component consists mainly of high-wavenumber modes. In fact, the power spectrum in the high-wavenumber region is mostly covered by the SGS component. However, although the SGS component is much smaller than the GS one at a low wavenumber, its level is rather higher than at a high wavenumber. Regarding this topic, a notable report was given by Piomelli *et al.*[24] that there is a significant difference in simulations between the Gaussian filter and the sharp cutoff filter. It is well known that the top-hat filter generally has a trend similar to that of the Gaussian filter. Therefore, if we use the top-hat filter in LES, the low-wavenumber range involved in the SGS component may affect flow simulations.

III. TURBULENCE MODELS TESTED IN THIS STUDY

We now briefly describe the SGS models investigated in this study.

A. *A priori* test using the true SGS stress obtained from finest-grid data

Knowing the correct model prediction is very useful for discussing model performance quantitatively. For this, we decomposed the finest-grid data (C395A) into the GS and SGS components

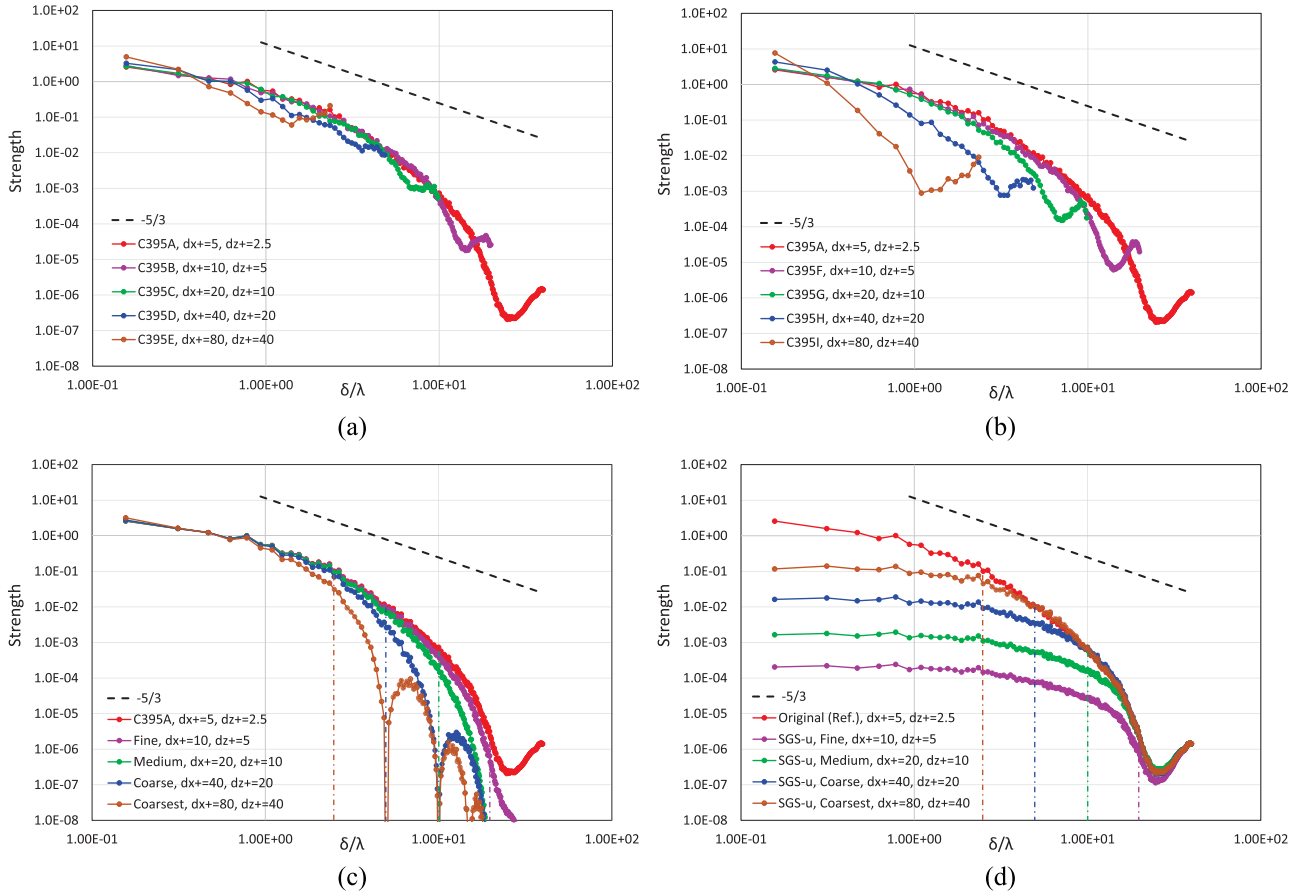

FIG. 3. Energy spectra of the streamwise velocity at $y^+ = 20$ for various grid resolutions: (a) SMM results, (b) EVM results, (c) *a priori* test (top-hat filter) of GS velocity using C395A, and (d) *a priori* test (top-hat filter) of SGS velocity using C395A. The finest-grid case (C395A) is included in all figures for reference. The dashed-dotted line in (c) and (d) denotes the filter width corresponding to the case in the same color.

through grid-filtering using the top-hat filtering operator. Note that, according to Horiuti,[9] we applied the filtering operator in the homogeneous directions (the x- and z-directions). We selected four grid-filter widths corresponding to the resolutions for the fine-, medium-, coarse-, and coarsest-grid cases in Table I. In this study, we evaluated the true values of the SGS stress using the original definition in Eq. (2) ($\tau_{true\,ij}$ hereafter).

B. Conventional linear eddy-viscosity model

To compare the characteristics of conventional SGS frameworks, two EVMs were tested: the SM[1] and the DSM.[2,3] The canonical form of a linear EVM is

$$\tau_{ij}{}^{a} = -2\,\nu_{SGS}\,S_{ij}, \tag{7}$$

where ν_{SGS} is the SGS eddy viscosity. In the SM, ν_{SGS} is modeled,

$$\nu_{SGS} = (C_S f_S \Delta)^2 \sqrt{2S^2}, \qquad f_S = 1 - \exp\left(-\frac{y^+}{A}\right), \tag{8}$$

where $S^2 = S_{ij}S_{ij}$. In Eq. (8), $C_S = 0.1$ and $A = 25$ are generally used constants. In contrast, ν_{SGS} in the DSM is

$$\nu_{SGS} = C\Delta^2\sqrt{2S^2}, \tag{9}$$

where the coefficient C is locally determined using the dynamic procedure proposed by Germano *et al.*[2] together with the least square approximation of Lilly.[3]

C. Anisotropy-resolving SGS model

To learn more about SGS model effects in LES, we then investigated an anisotropic SGS model originally proposed by Abe.[16] This model is constructed by combining an isotropic EVM with an EAT. The SGS stress is modeled as

$$\tau_{ij}{}^{a} = -2\,\nu_{SGS}\,S_{ij} + 2\,k_{SGS}\,b_{ij}^{EAT} = EVM_{ij} + EAT_{ij}, \tag{10}$$

where k_{SGS} is the SGS turbulence energy defined as $k_{SGS} = \tau_{kk}/2$ in this study. The anisotropy tensor b_{ij}^{EAT} in the EAT of Eq. (10) is

modeled as

$$b_{ij}^{EAT} = \frac{\tau'_{ij} - \left(-2\nu' S_{ij}\right)}{\tau'_{kk} - \left(-2\nu' S_{kk}\right)} - \frac{1}{3}\delta_{ij} = \frac{\tau'^{a}_{ij} - \left(-2\nu' S_{ij}\right)}{\tau'_{kk}}, \qquad (11)$$
$$\nu' = -\frac{\tau'^{a}_{ij} S_{ij}}{2S^2}, \quad \tau'_{ij} = \left(\overline{U}_i - \widehat{\overline{U}}_i\right)\left(\overline{U}_j - \widehat{\overline{U}}_j\right),$$

where $\tau'^{a}_{ij} = \tau'_{ij} - \tau'_{kk}\delta_{ij}/3$. In Eq. (11), ν' is an equivalent eddy viscosity obtained using an EVM-type linear approximation for $\tau_{ij}{}'$, which is given by the scale-similarity model of Bardina *et al.*[8] Note that $\widehat{(\ )}$ denotes a test-filtered value. Further details of this SGS model are given in the reference paper.[16]

Considering that the EAT in Eq. (11) yields no undesirable extra energy transfer between the GS and SGS components, we expect this anisotropic SGS model to successfully predict the SGS-stress anisotropy with no significant effect on computational stability. In this sense, this SGS model is regarded as a combination of a linear EVM[25] and a scale-similarity model effectively modified for stable computation, hence the name "stabilized mixed model" (SMM).

To clarify the role of the EAT in the SMM, we also investigated an isotropic EVM version consisting of only the first term on the right side of Eq. (10). This isotropic version is referred to as "EVM" described in Table I.

IV. RESULTS AND DISCUSSION

A. Budget of GS Reynolds stress

To validate the quality of our simulation with a sufficient grid resolution, Fig. 4 compares the budget quantities of $\langle u''v'' \rangle$ for the finest-grid data (C395A). Figure 4(a) compares the long-time averaged data with those of the DNS,[21] while Fig. 4(b) shows the results obtained only from the plane-averaged data at an instantaneous time step. The latter confirmation is important because we need to use the reference data for comparison in the following *a priori* tests, for which we have to produce filtered data for all budget terms using the finest-grid data at an instantaneous time step. Because this plane-averaging procedure has often been used for *a priori* tests in many studies,[2,11,13] it is generally useful. However, the number of sample data used for a plane-averaged value is much lower than that for a long-time averaged one. Therefore, to reveal how the number of sample data affects the analysis, we compare the distributions obtained with these two procedures in Fig. 4(b).

As seen in Fig. 4(a), the simulation results show good agreement with the DNS data for all budget quantities. This confirms the basic quality of our LES with sufficient grid resolution. Also, the plane-averaged data reasonably agree with the long-time averaged data in Fig. 4(b). The plane-averaged data show no significant discrepancy with the long-time averaged ones, although statistical convergence is not perfect and some wavy profiles remain. Note that we intentionally exclude the effects of the SGS stress from the plane-averaged results. The fact that the balance is sufficiently maintained only by the GS data confirms that the SGS stress has almost no effect on the budget for the finest-grid case.

This validation means that we can successfully produce filtered budget data for coarser grids, using the finest-grid data with filtering. We then calculate the budget of the GS *Re* shear stress, $\langle u''v'' \rangle$,

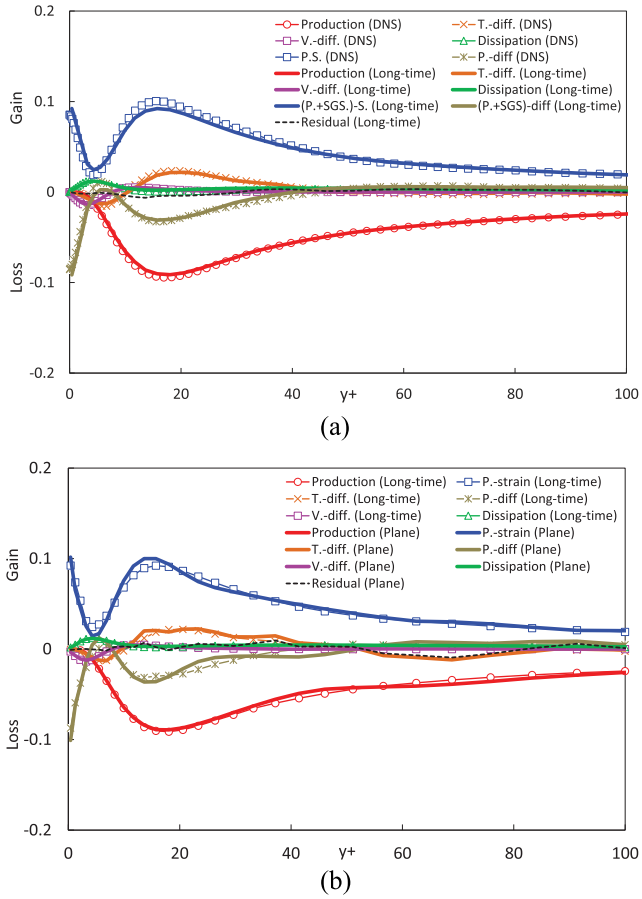

FIG. 4. Budget of *Re* shear stress for the finest-grid case (C395A) (P.S.: pressure-strain; T.-diff.: turbulent diffusion; P.-diff.: pressure diffusion; V.-diff.: viscous diffusion; SGS-diff.: SGS diffusion; SGS-S.: SGS-strain): (a) comparison of long-time averaged and DNS[21] data and (b) comparison of plane-averaged and long-time averaged data. All budget terms are normalized by the wall unit.

for the fine, medium, coarse, and coarsest grids in Table I. Figure 5 compares the results calculated from the filtered values with those from the original finest-grid data. All budget terms tend to decrease as the grid becomes coarser. Considering the results in Fig. 2, this seems a natural consequence of the change in grid resolution. Thus far, however, we have not known how the results should behave when grid resolution decreases, so the present results including all terms in Eq. (4) are very important for determining the performance of an SGS model for coarse grids. We treat these filtered data as the reference values to be reproduced for the corresponding grid resolution. Henceforth, we call these reference values the "true values" for convenience, although their quality is not always perfect.

In this study, we focus especially on the SGS-strain term ξ_{12} in Eq. (4). We discuss how ξ_{12} behaves in the budget as the grid resolution decreases. We also study the pressure-strain term ϕ_{12} in Eq. (4) because ϕ_{12} is one of the main budget contributors. If we consider a statistically steady-state plane channel flow taking $i = 1$ and $j = 2$ in

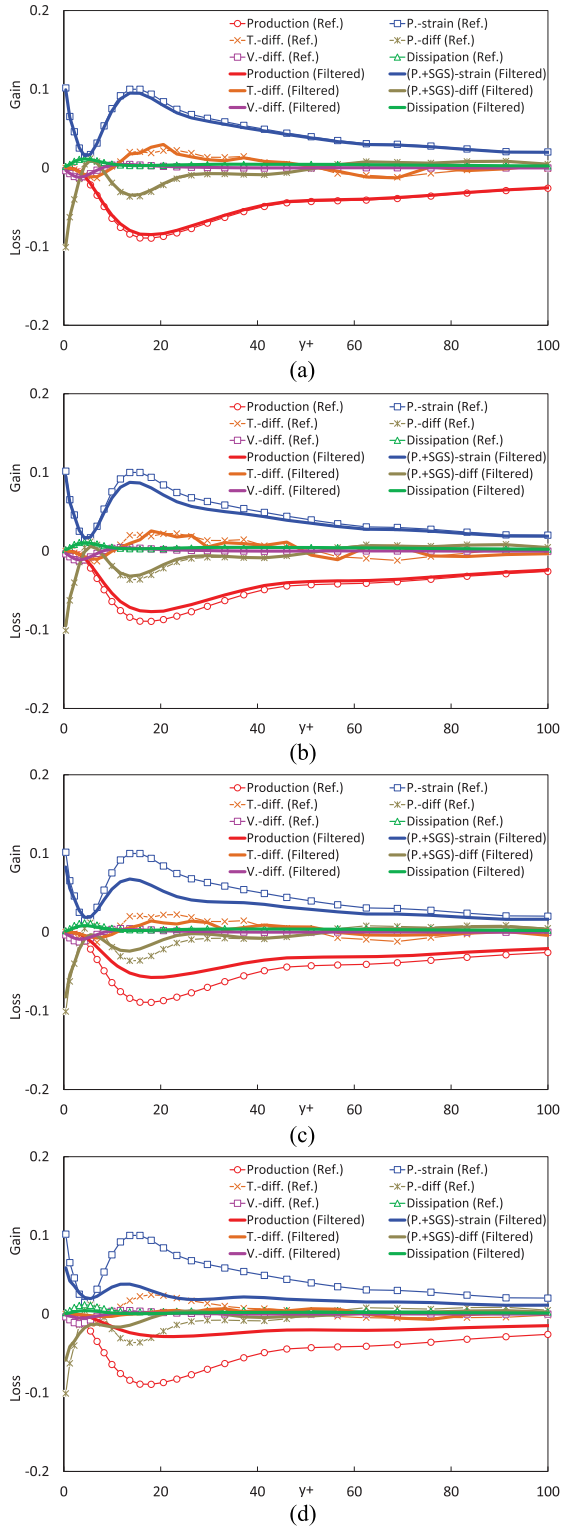

FIG. 5. Budget of GS *Re* shear stress for various grid resolutions: (a) fine, (b) medium, (c) coarse, and (d) coarsest. The finest grid results (C395A) are included for reference.

Eq. (5), ϕ_{12} and ξ_{12} are expressed as

$$\phi_{12} = \left\langle \frac{p''}{\rho}\left(\frac{\partial u''}{\partial y} + \frac{\partial v''}{\partial x}\right)\right\rangle,$$
$$\xi_{12} = \left\langle \left(\tau_{xx}^{a\,\prime\prime}\frac{\partial v''}{\partial x} + \tau_{xy}^{a\,\prime\prime}\frac{\partial v''}{\partial y} + \tau_{xz}^{a\,\prime\prime}\frac{\partial v''}{\partial z}\right) + \left(\tau_{yx}^{a\,\prime\prime}\frac{\partial u''}{\partial x} + \tau_{yy}^{a\,\prime\prime}\frac{\partial u''}{\partial y} + \tau_{yz}^{a\,\prime\prime}\frac{\partial u''}{\partial z}\right)\right\rangle. \quad (12)$$

As seen in Eq. (12), both ϕ_{12} and ξ_{12} involve instantaneous fluctuation of the velocity gradient. Also, considering that p''/ρ is originally $(p''/\rho)\delta_{ij}$, the formulations of ϕ_{12} and ξ_{12} are basically similar, and thus, ξ_{12} is expected to work in conjunction with ϕ_{12}.

Figure 6 shows the distributions of ϕ_{12} and ξ_{12} as well as their total $(\phi_{12} + \xi_{12})$ for the fine, medium, coarse, and coarsest grids. The effect of ξ_{12} increases as the grid resolution becomes coarser. For the coarsest-grid case in Fig. 6(d), ξ_{12} is significant near the wall at around $y^+ = 20$. As stated before, we regard these as the reference distributions to be reproduced for the corresponding grid resolution. We next perform *a priori* tests for ξ_{12} with several SGS models using the filtered data. We calculate ξ_{12} in each SGS model and compare the results with the reference data. The primary concern is how well each SGS model works for reproducing the ξ_{12} distributions in Fig. 6. We also investigate in detail the role of the EAT in predictive accuracy of an SGS model.

B. Isotropic and anisotropic contributions of the true SGS stress to the SGS-strain term

We further discuss the true values of ξ_{12} in Fig. 6. As mentioned in Sec. III, using the equivalent eddy viscosity to decompose an SGS-stress tensor into the isotropic EVM and the remaining component is very effective in investigating model performance because such an EVM part has exactly the same amount of the energy transfer between the GS and SGS parts at any point. Therefore, we introduce this procedure to the true SGS stress obtained from the filtered data as follows:

$$\tau_{true\ ij}^{\ a} = EVM_{true\ ij} + EAT_{true\ ij} = -2\,\nu_E\,S_{ij} + EAT_{true\ ij}. \quad (13)$$

In Eq. (13), ν_E is the equivalent eddy viscosity calculated using an EVM-type linear approximation for the true SGS-stress tensor as follows:

$$\tau_{true\ ij}^{\ a}\,S_{ij} = -2\nu_E S_{ij}S_{ij} \longrightarrow \nu_E = -\frac{\tau_{true\ ij}^{\ a}\,S_{ij}}{2S^2}. \quad (14)$$

The residual is regarded as the anisotropic part of the true SGS stress defined as

$$EAT_{true\ ij} = \tau_{true\ ij}^{\ a} - (-2\,\nu_E\,S_{ij}). \quad (15)$$

As found from Eq. (14), the isotropic part $EVM_{true\ ij}$ using ν_E completely reproduces the energy transfer between the GS and SGS parts including both the forward and backward scatters. We regard ν_E as the ideal distribution of the SGS eddy viscosity (ν_{SGS}) to be reproduced by an SGS model. Therefore, investigating the performance of $EVM_{true\ ij}$ should show us a basic potential of an isotropic EVM-type SGS model for predicting ξ_{12}.

By using $EVM_{true\ ij}$ and $EAT_{true\ ij}$, we decompose ξ_{12} into its isotropic and anisotropic parts as follows:

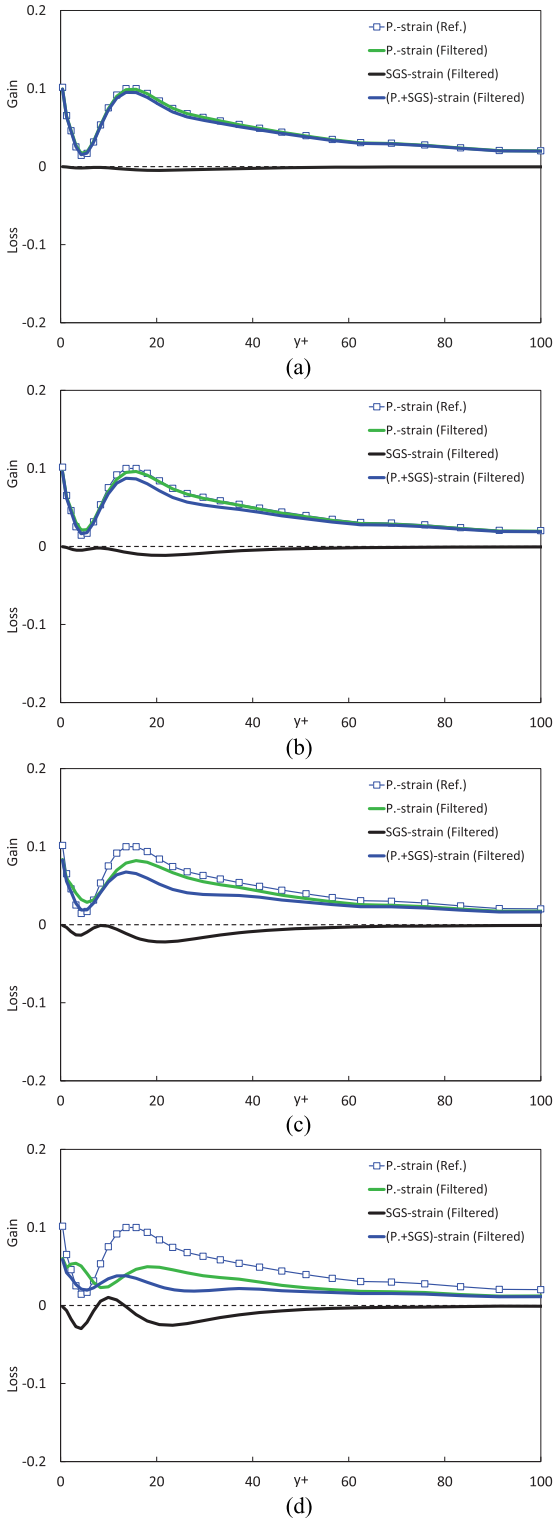

FIG. 6. Contribution of the SGS-strain term to the pressure-strain term for various grid resolutions: (a) fine, (b) medium, (c) coarse, and (d) coarsest. The finest grid results (C395A) are included for reference.

$$\xi_{12} = \xi_{12}^{EVM} + \xi_{12}^{EAT}, \tag{16}$$

where

$$\xi_{12}^{EVM} = \left\langle EVM_{1k}'' \frac{\partial v''}{\partial x_k} + EVM_{2k}'' \frac{\partial u''}{\partial x_k} \right\rangle, \tag{17}$$

$$\xi_{12}^{EAT} = \left\langle EAT_{1k}'' \frac{\partial v''}{\partial x_k} + EAT_{2k}'' \frac{\partial u''}{\partial x_k} \right\rangle. \tag{18}$$

Figure 7 shows the results for ξ_{12}^{EVM} at various grid resolutions, and Fig. 8 shows those for ξ_{12}^{EAT}. Note that in these *a priori* tests, the ϕ_{12} distributions shown in green are the same for a fixed grid resolution. The figure shows definite differences between the ξ_{12}^{EVM} and ξ_{12}^{EAT} distributions, particularly for the coarse and coarsest grids.

Surprisingly, $EVM_{true\ ij}$ in Fig. 7 has little or no effect on the ξ_{12} prediction. This may be a major problem for a linear EVM-type SGS model. Because $EVM_{true\ ij}$ completely includes both the forward and backward scatters, this shows that even perfectly reproducing the energy transfer between the GS and SGS parts may not improve the predictive accuracy of the $\langle u''v'' \rangle$ budget for coarse grids.

In contrast, ξ_{12}^{EAT} in Fig. 8 yields distributions that correspond fairly well to the true values. This means that most of ξ_{12} is actually generated by the anisotropic part of the SGS stress. It is noted again that $EAT_{true\ ij}$ yields no energy transfer between the GS and SGS components because this term is a residual after subtracting an equivalent eddy-viscosity form from the original true SGS stress [Eq. (15)]. Note that detailed investigation of each term in Eq. (18) revealed a remarkable correlation between EAT_{22}'' and $\partial u''/\partial y$. Because no such effect is seen in the other combinations, this correlation is the main contributor to ξ_{12}.

These investigations provide the following important information. The difference between Figs. 7 and 8 shows that a linear EVM approximation of the true SGS stress using ν_E cannot reasonably predict ξ_{12}, even if both the forward and backward scatters are included in the SGS eddy viscosity. Furthermore, a strong correlation between EAT_{22}'' and $\partial u''/\partial y$ indicates that accurately predicting ξ_{12} requires reproduction of the SGS-stress anisotropy. The anisotropic part in Eq. (15) works well for this purpose, although it provides neither forward nor backward scatter. The information obtained here may lead to further improvement in predicting the GS *Re* shear stress, resulting in more accurate mean-velocity predictions for coarse grids.

C. *A priori* tests of several SGS models

To confirm the information obtained in Sec. IV B, we perform the same *a priori* tests using the SGS models described in Sec. III.

The SM[1] and the DSM[2] have often been used in engineering applications, so we study the performances of these two conventional linear SGS models by using them in the next *a priori* tests. Figure 9 shows the ξ_{12} distributions predicted by the SM, and Fig. 10 shows those by the DSM. Both the SM and the DSM have little or no value for ξ_{12}, resulting in a total $(\phi_{12} + \xi_{12})$ different from that of the true value.

Next, the anisotropic SGS model of Abe[16] (SMM) is used in these *a priori* tests. Note that its isotropic version (EVM) is also tested for comparison. Figure 11 shows the ξ_{12} distributions

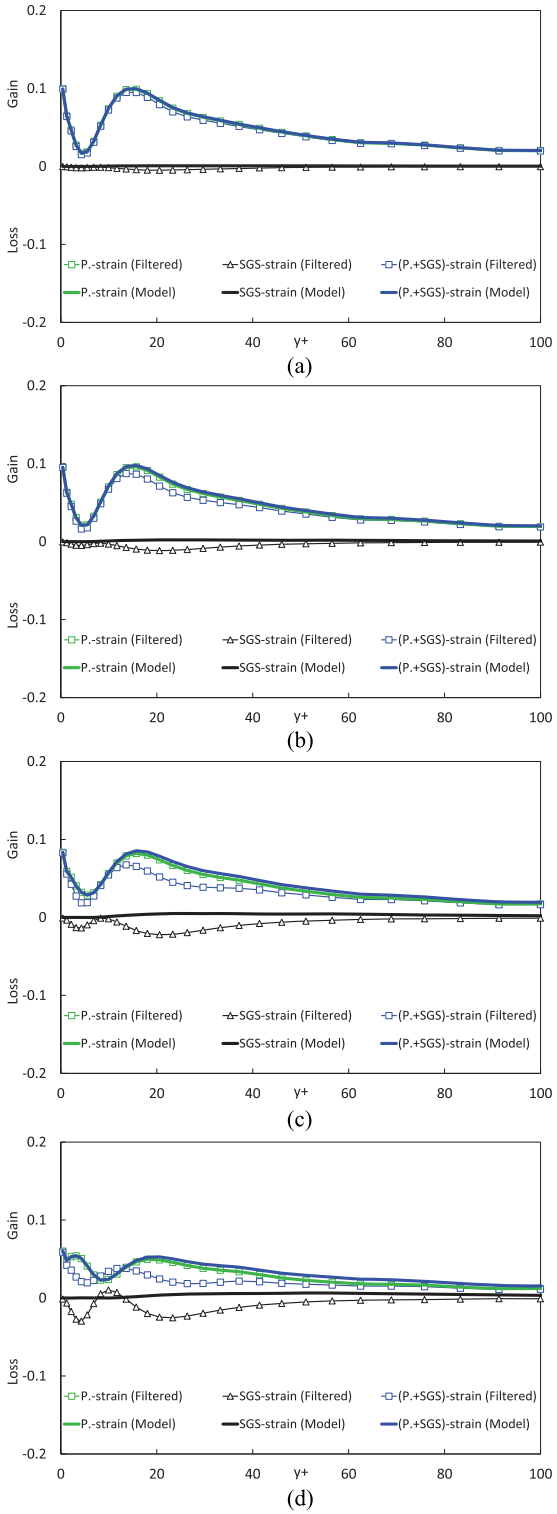

FIG. 7. Contribution of the isotropic term ξ_{12}^{EVM} in the SGS-strain term to the budget of the GS *Re* shear stress. The black lines represent ξ_{12}^{EVM} [Eq. (17)] using ν_E [Eq. (14)]: (a) fine, (b) medium, (c) coarse, and (d) coarsest.

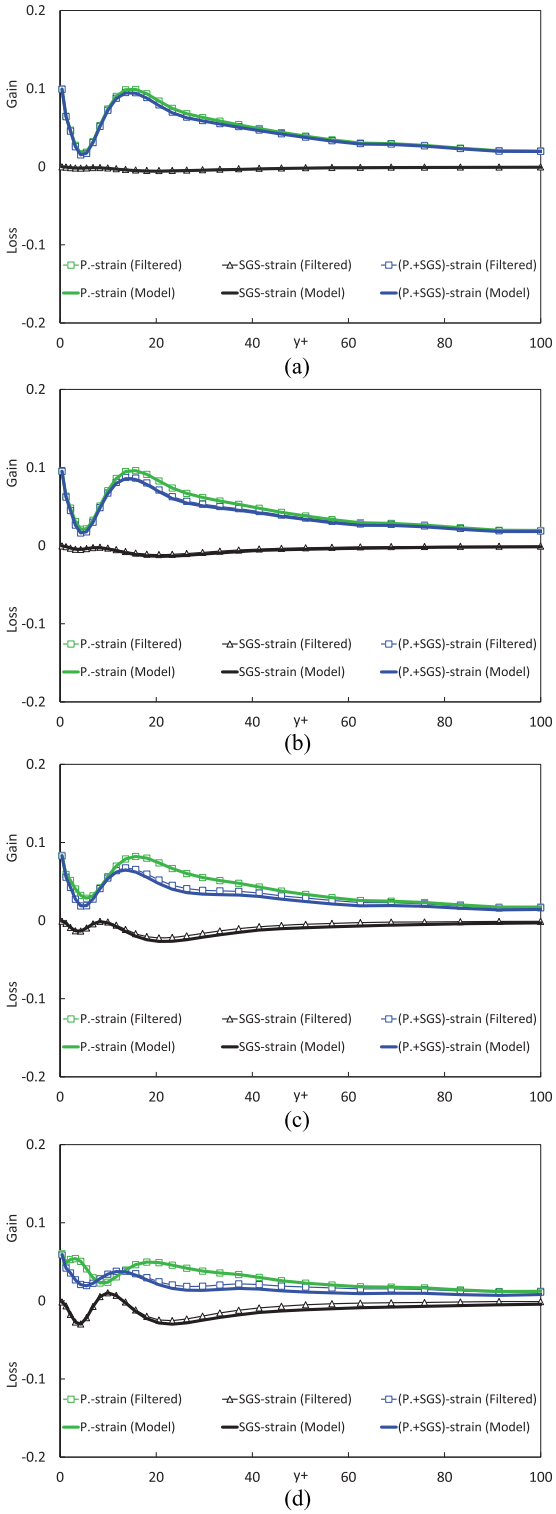

FIG. 8. Contribution of the anisotropic term ξ_{12}^{EAT} in the SGS-strain term to the budget of the GS *Re* shear stress. The black lines represent ξ_{12}^{EAT} [Eq. (18)] using EAT_{true} [Eq. (15)]: (a) fine, (b) medium, (c) coarse, and (d) coarsest.

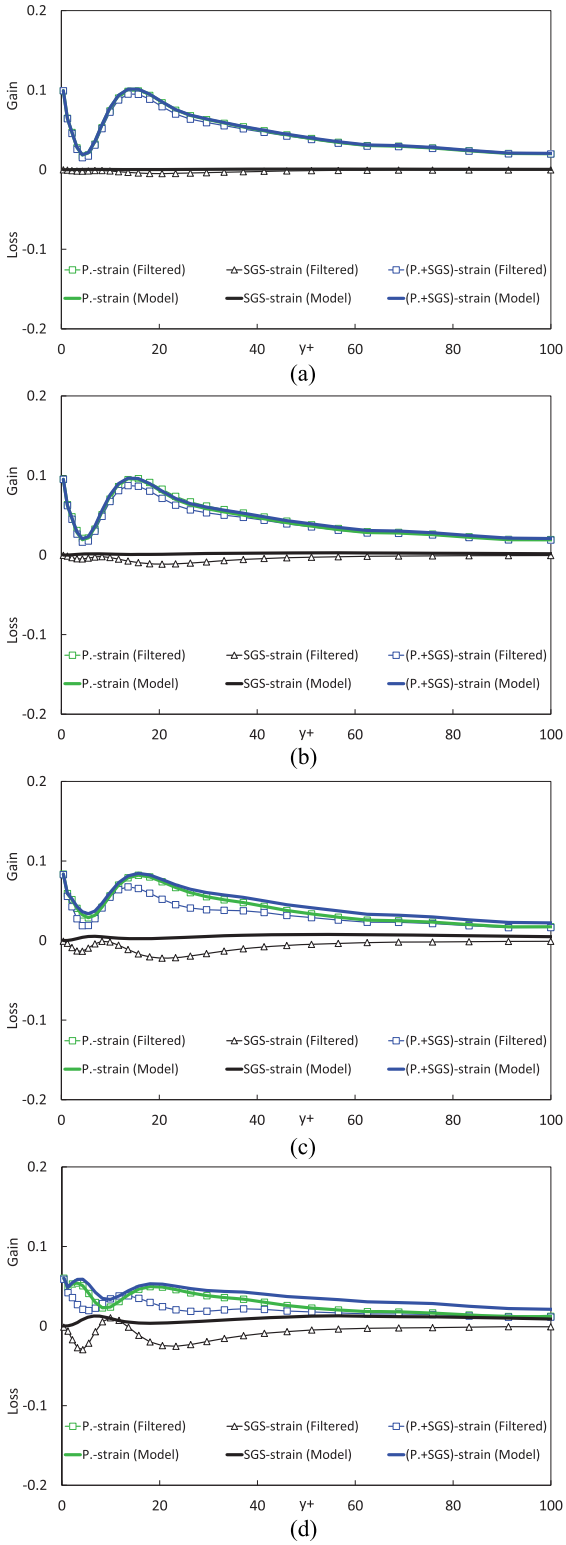

FIG. 9. *A priori* test of SM using the filtered coarse-grid values: (a) fine, (b) medium, (c) coarse, and (d) coarsest.

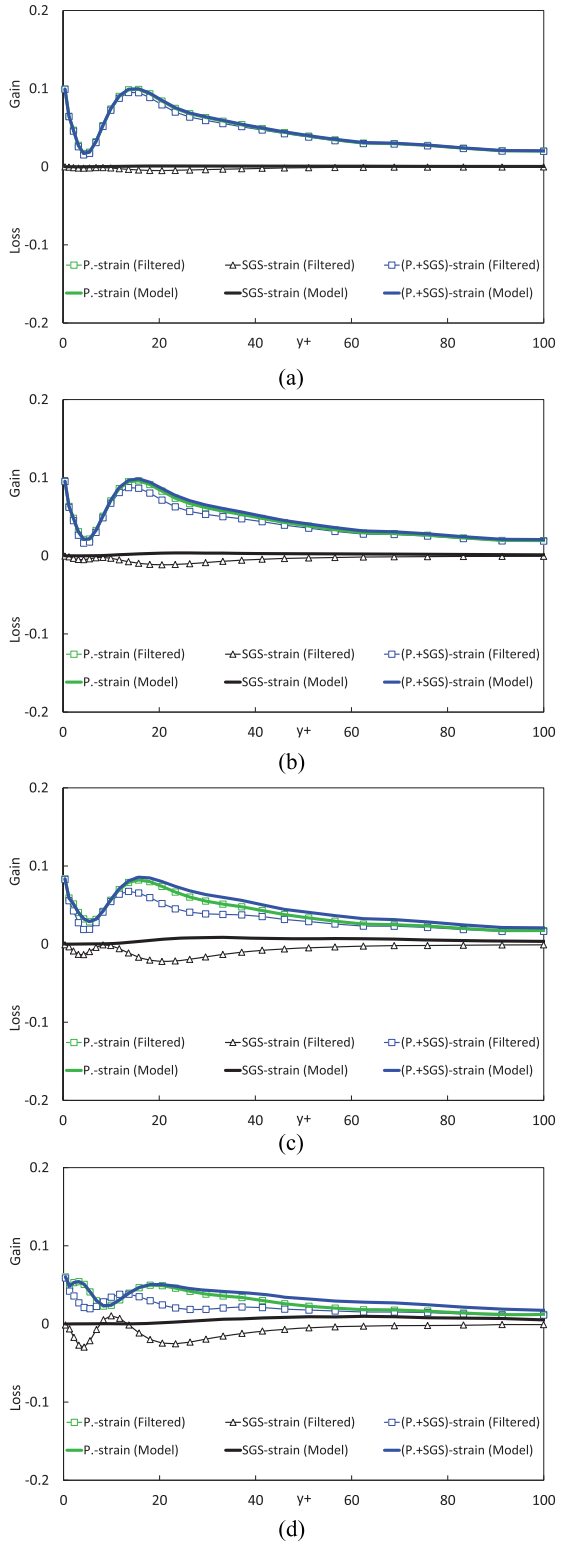

FIG. 10. *A priori* test of DSM using the filtered coarse-grid values: (a) fine, (b) medium, (c) coarse, and (d) coarsest.

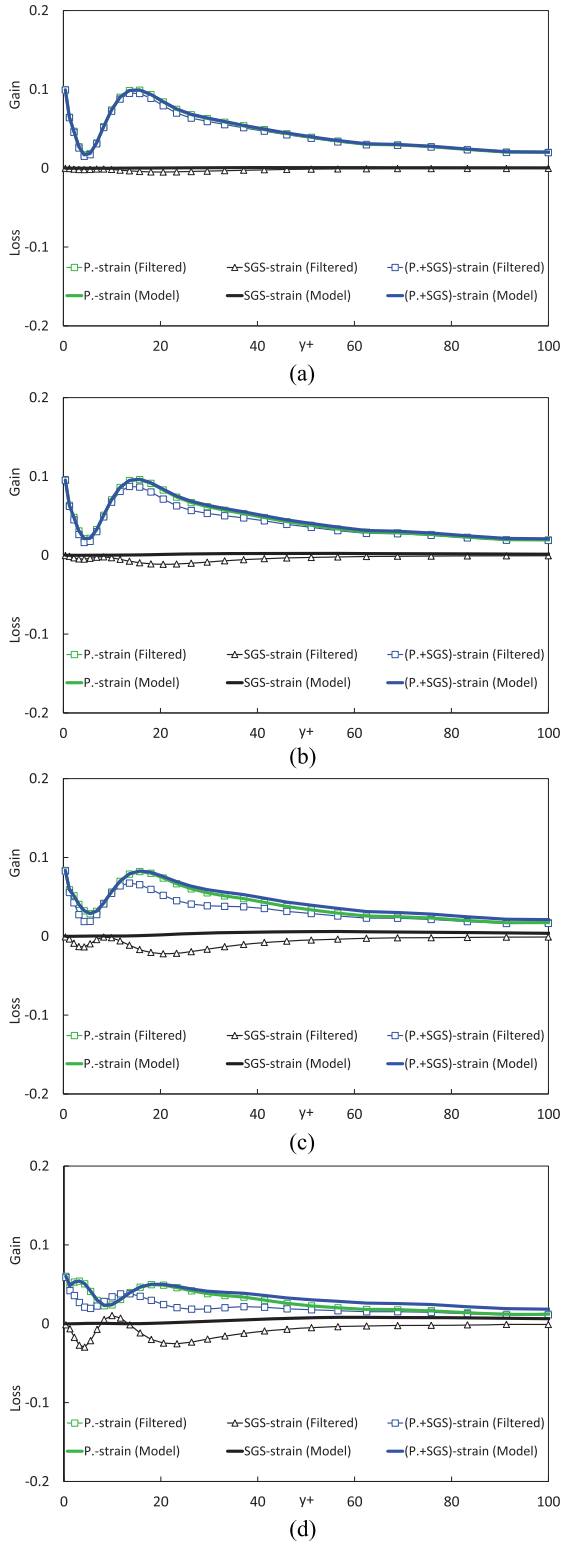

FIG. 11. *A priori* test of EVM using the filtered coarse-grid values: (a) fine, (b) medium, (c) coarse, and (d) coarsest.

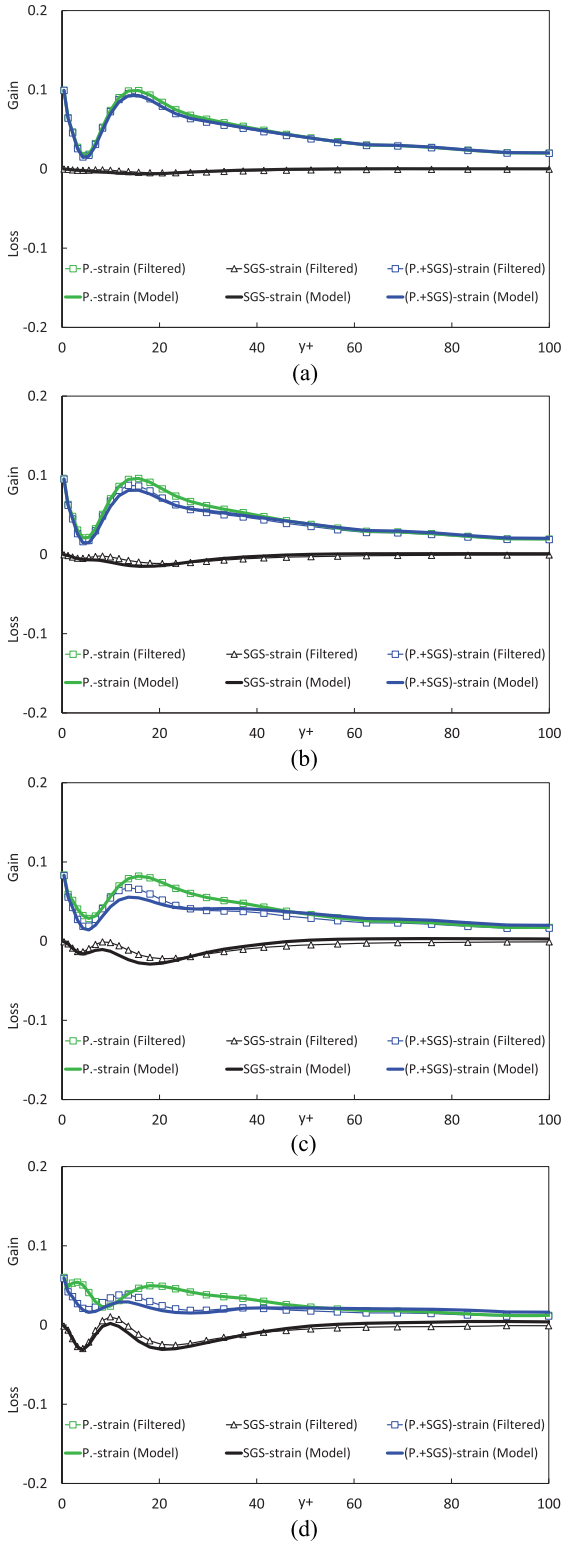

FIG. 12. *A priori* test of SMM using the filtered coarse-grid values: (a) fine, (b) medium, (c) coarse, and (d) coarsest.

predicted by the EVM, and Fig. 12 shows those by the SMM. In the EVM results of Fig. 11, ξ_{12} has almost no value even if the grid resolution becomes coarse. This is similar to what was found for the results by other EVM-type SGS models. In contrast, the SMM yields significant ξ_{12} distributions that show generally good agreement with the true values, although there are still some discrepancies. As a result, the total $(\phi_{12} + \xi_{12})$ from the SMM also shows much better agreement with the true values than that of the EVM.

The information obtained here shows no disagreement with that obtained from the true values in Sec. IV B. The EVM part in an SGS model does not work properly for providing a reasonable ξ_{12} distribution in the GS field, although it is necessary as a part of the production term for k_{SGS} in the SGS field. We therefore expect an anisotropy-resolving SGS model to improve the predictive accuracy not only for the SGS part $\langle \tau_{ij} \rangle$ but also for the GS part $\langle u_i'' u_j'' \rangle$ through its budget. A better prediction of both $\langle \tau_{ij} \rangle$ and $\langle u_i'' u_j'' \rangle$ directly leads to an improved mean-velocity prediction. This may be why the SMM shows relatively low grid dependency compared with isotropic EVM-type SGS models, as shown in Fig. 1.

D. *A posteriori* tests of the present anisotropic SGS model

From the aforementioned *a priori* tests, we obtained useful knowledge about how an SGS model should work for improving the prediction accuracy for coarse-grid resolutions. The investigations indicated that introducing an anisotropic term is very effective for further improvement of the LES performance. In a real calculation, however, several factors may influence the computational results. Therefore, in this section, we calculate the terms in the $\langle u'' v'' \rangle$ budget using the results of *a posteriori* tests for various grid resolutions at $Re_\tau = 395$, as detailed in Table I. We then compare the predictions with the filtered true data for the corresponding grid resolutions, respectively.

Figure 13 shows the ξ_{12} distributions obtained from the results of *a posteriori* tests by the EVM, and Fig. 14 shows those obtained by the SMM. It can be seen that ξ_{12} has almost no value in the EVM results. A comparison between Figs. 11 and 13 reveals that the pressure-strain term considerably decreases in the real calculation as the grid resolution coarsens. It is considered that this decrease of the pressure-strain term in the real calculation results in the decline of the prediction accuracy for coarse-grid cases.

In contrast, Fig. 14 shows that the SMM returns definite ξ_{12} distributions in the real calculations. For the fine- and medium-grid cases, the ξ_{12} distributions predicted by the SMM generally show reasonable agreement with the results of *a priori* tests, although some discrepancies are still seen in the medium-grid case. Concerning the coarse- and coarsest-grid cases, the SMM considerably overpredicts in the region close to the wall surface (i.e., $y^+ < 10$). Although the values of ξ_{12} predicted by the SMM are generally considered to contribute to the improvement of the mean-velocity prediction, such an error in the real calculation should be reduced; thus, further detailed investigation is necessary.

E. Higher Reynolds-number cases

Finally, we investigate the model performance for higher Re cases (Re_τ = 1000, 2000). Figure 15 shows the mean-velocity

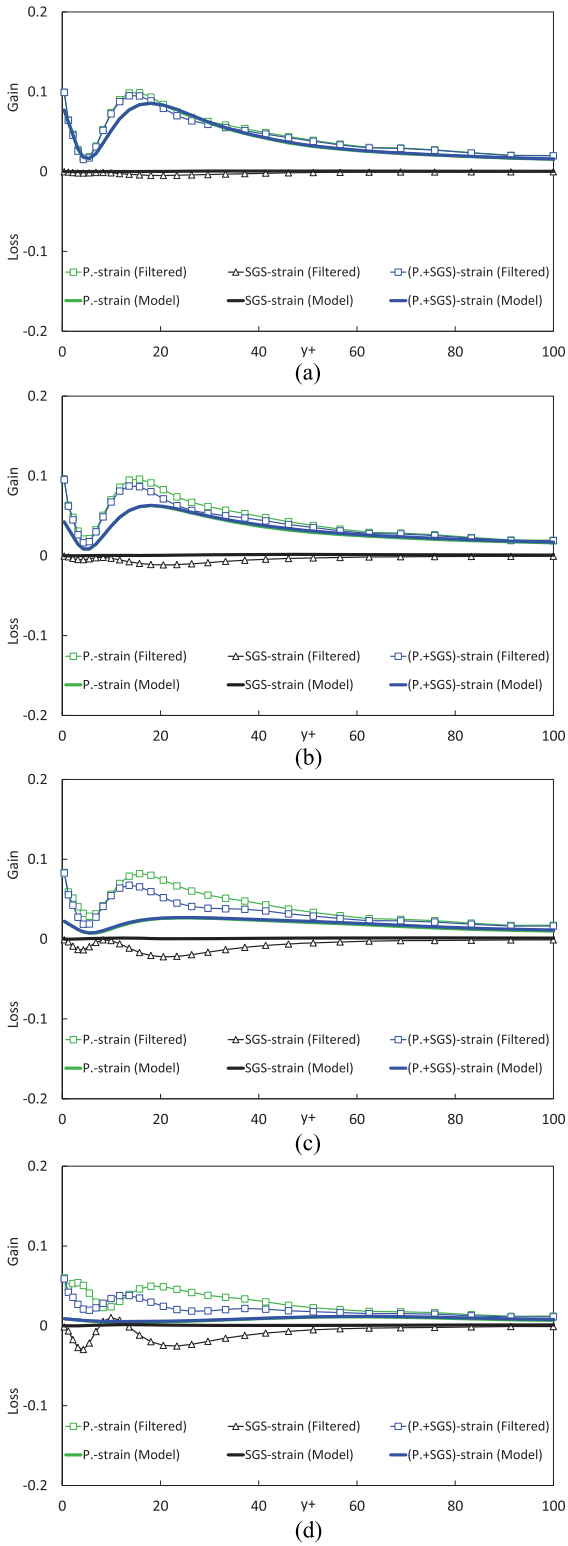

FIG. 13. *A posteriori* test of EVM: (a) fine, (b) medium, (c) coarse, and (d) coarsest.

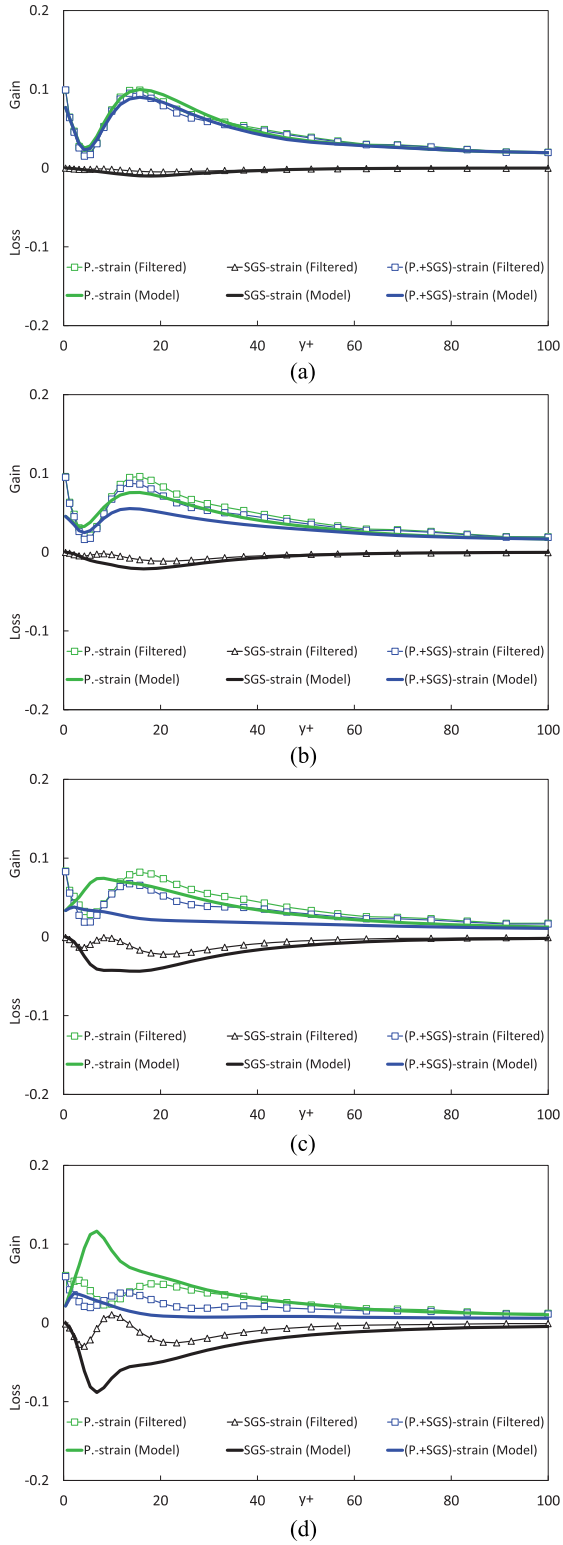

FIG. 14. *A posteriori* test of SMM: (a) fine, (b) medium, (c) coarse, and (d) coarsest.

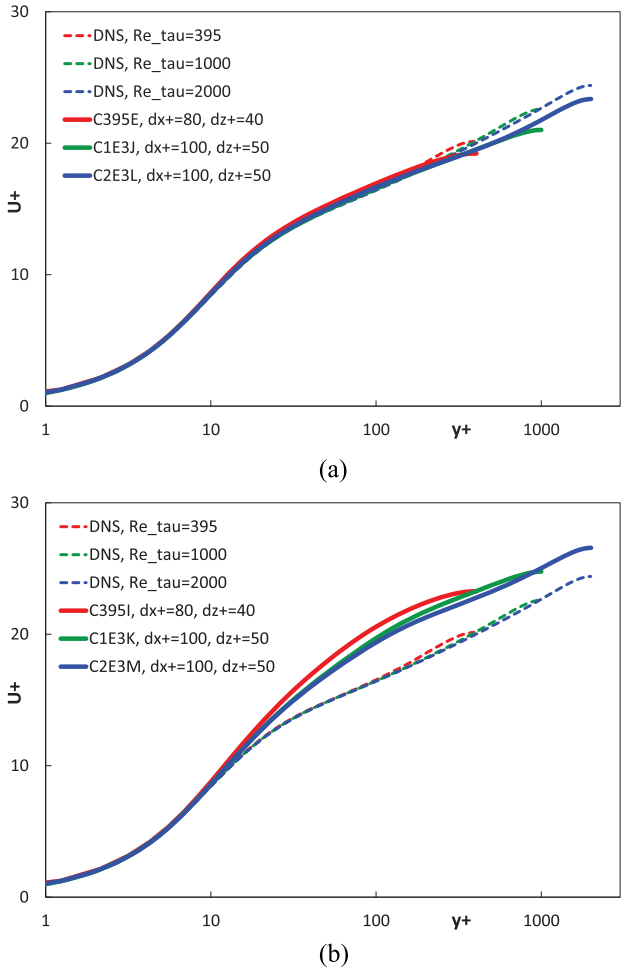

FIG. 15. Mean-velocity predictions for higher Reynolds numbers: (a) SMM and (b) EVM.

distributions obtained by the SMM and the EVM. Note that in the figure, the results for C395E and C395I are also included for reference because their grid resolution in the wall unit is similar to that of the higher *Re* cases. The predicted U_b^+ and C_f are compared with the corresponding DNS data[22] in Table III.

TABLE III. Comparison of the bulk-mean velocity U_b^+ and the friction coefficient C_f with the DNS data[22] for higher *Re* cases.

Case	Model	Re_τ	U_b^+	Error (%)	C_f	Error (%)
DNS[22]		1000	19.99		5.01×10^{-3}	
C1E3J	SMM	1000	19.15	−4.21	5.46×10^{-3}	8.99
C1E3K	EVM	1000	22.69	13.52	3.88×10^{-3}	−22.40
DNS[22]		2000	21.80		4.21×10^{-3}	
C2E3L	SMM	2000	21.06	−3.39	4.51×10^{-3}	7.15
C2E3M	EVM	2000	24.24	11.19	3.40×10^{-3}	−19.11

As shown in Fig. 15(b), the EVM provides considerable over-predictions, where the results shift upward from the DNS data. This is a well-known feature that was already seen in coarse grid resolutions at $Re_\tau = 395$.

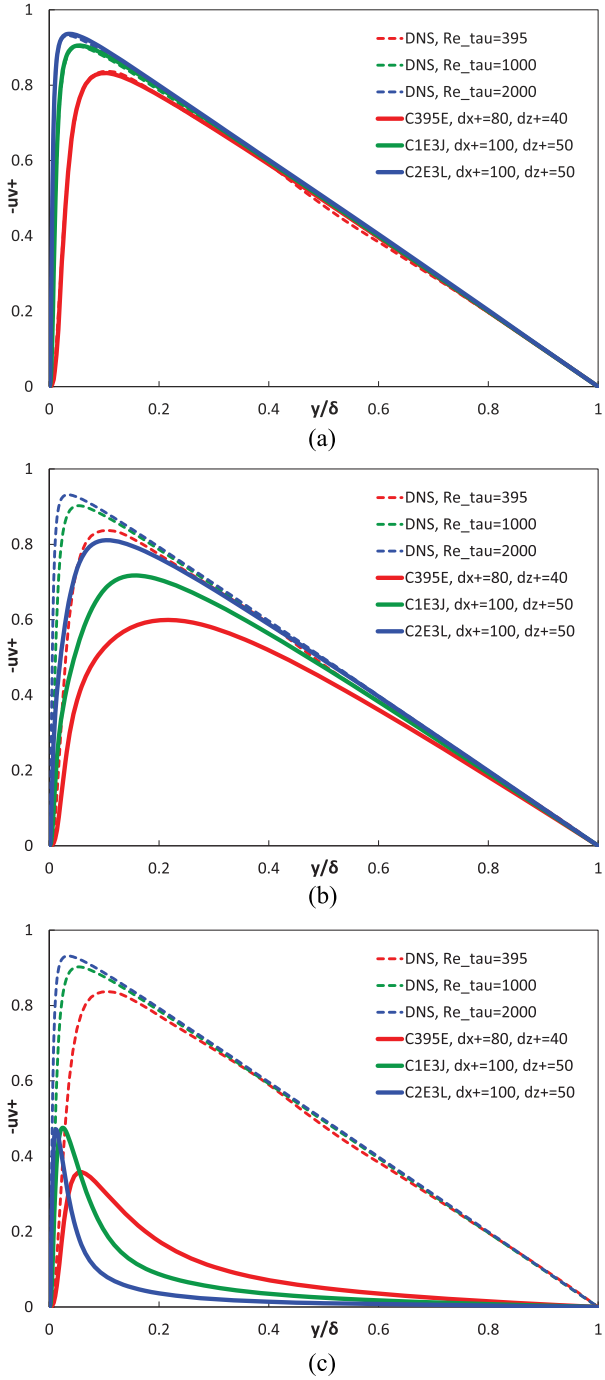

FIG. 16. Total (GS + SGS), GS, and SGS *Re* shear stress calculated by SMM for higher Reynolds numbers: (a) total (GS + SGS) *Re* shear stress, (b) resolved GS part, $\langle u''v'' \rangle$, and (c) modeled SGS part, $\langle \tau_{12} \rangle$.

In contrast, the trend of the SMM is clearly different from that of the EVM. The SMM generally returns reasonable predictions of the mean velocity for all *Re* cases, although slight under-predictions are seen in the logarithmic region. In general, such an

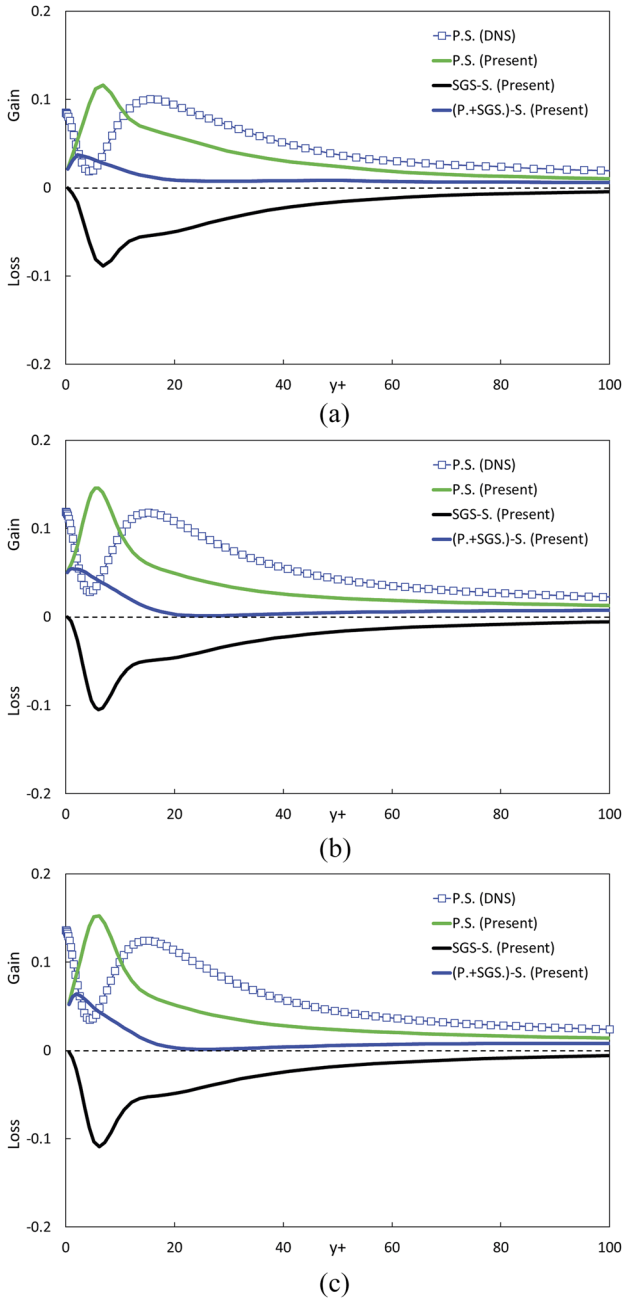

FIG. 17. *A posteriori* test of SMM for higher Reynolds numbers: (a) C395E, (b) C1E3J, and (c) C2E3L. Because the filtered true values are not available for higher *Re* cases (b) and (c), the original pressure-strain term corresponding to each test case is included for comparison. The results in (a) for C395E are the same as those in Fig. 14(d).

improvement of the prediction accuracy indicates a reasonable prediction of the mean-friction coefficient. This is quantitatively confirmed in Table III.

Figure 16 shows the *Re* shear stress predicted by the SMM. The feature in the mean-velocity predictions is reasonably explained from Fig. 16(a), where the total (GS + SGS) values predicted by the SMM generally show good agreement with the corresponding DNS data. As is similar to the cases at $Re_\tau = 395$, the balance between the GS and SGS parts changes according to the flow conditions.

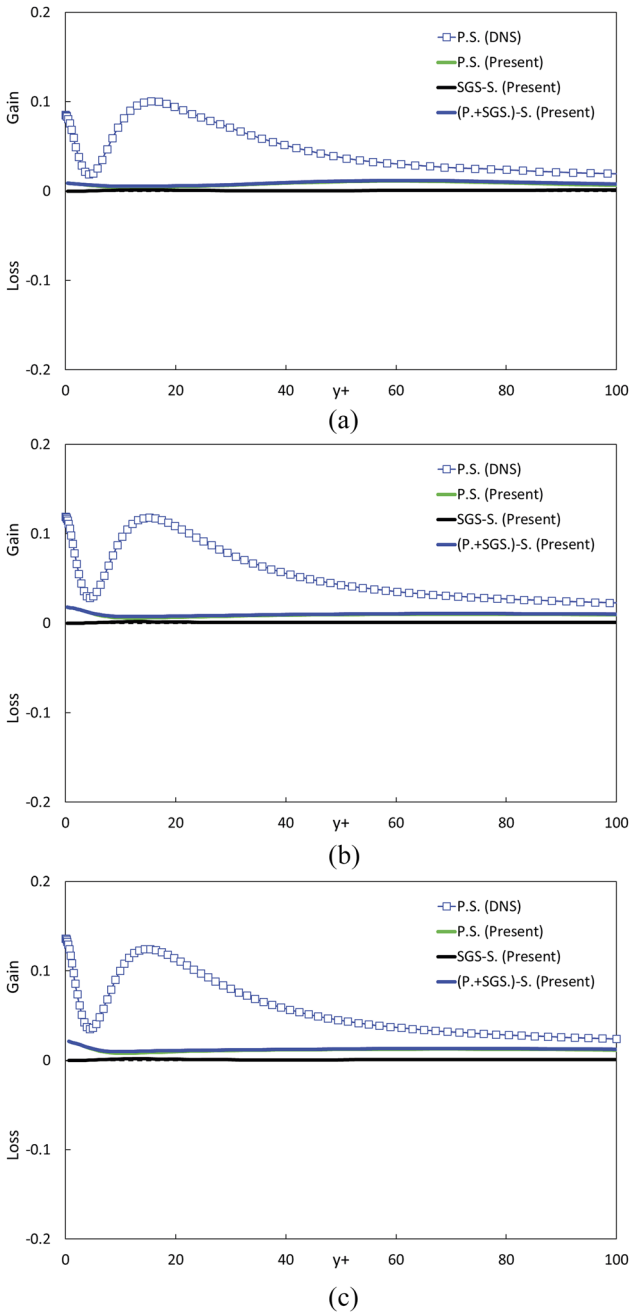

FIG. 18. *A posteriori* test of EVM for higher Reynolds numbers: (a) C395I, (b) C1E3K, and (c) C2E3M. The results in (a) for C395I are the same as those in Fig. 13(d).

To investigate how the $\langle u''v'' \rangle$ budget in the near-wall region is affected by the Reynolds number, Fig. 17 compares the ξ_{12} distributions predicted by the SMM and Fig. 18 compares those by the EVM for various Reynolds numbers. Note that the filtered true values are not available for higher *Re* cases; thus, the original pressure-strain term corresponding to each test case is included for reference.

It is confirmed again that the EVM results of Fig. 18 have almost no value of ξ_{12} even if the Reynolds number becomes higher. In contrast, the SMM yields significant ξ_{12} distributions for higher *Re* cases, although the accuracy is still far from perfect. It is however interesting that very similar trend is obtained in the ξ_{12} distributions for all *Re* cases. Therefore, the obtained feature is expected to be seen not only in low *Re* flows but also in much higher *Re* flows. This also indicates that even an improvement of the model performance in the near-wall region at a low *Re* will make a contribution to further development of higher *Re* practical LES.

V. CONCLUDING REMARKS

In this study, we investigated the effect of the anisotropic term in an SGS model on predicting the resolved GS *Re* stress through its budget. We performed *a priori* tests using highly resolved LES data of a plane channel flow. We evaluated all budget terms of the GS *Re* shear stress for various coarse grids by filtering the simulation data for the finest grid. Among them, we focused on the contribution of a term closely related to the instantaneous fluctuation of the SGS stress. We compared the results of some conventional EVM-type SGS models and an anisotropy-resolving SGS model with the true values obtained from the filtered data.

Research so far on the SGS contribution to mean-velocity prediction has focused mainly on its ensemble average $\langle \tau_{12} \rangle$ appearing in the mean-velocity equation [Eq. (3)]. In this study, however, we have found that the instantaneous fluctuation of the SGS stress coupled with that of the GS velocity gradient largely affects the distribution of the resolved GS *Re* shear stress $\langle u''v'' \rangle$ through ξ_{12} in Eq. (4).

Because the $\langle u''v'' \rangle$ distribution is most important for predicting the mean velocity in a wall-shear flow, we carefully investigated the effect of ξ_{12} on the $\langle u''v'' \rangle$ budget. We decomposed ξ_{12} obtained from the filtered data into its isotropic and anisotropic parts. Their comparison showed that most of the contribution was given by the anisotropic part, while the isotropic part had little effect on predicting ξ_{12}. Because other conventional isotropic SGS models also showed little effect on its prediction, isotropic EVM-type SGS models essentially cannot improve the distribution of $\langle u''v'' \rangle$. This may be why an anisotropy-resolving SGS model greatly improves the mean-velocity prediction for coarse grids compared with conventional isotropic SGS models.

Furthermore, to validate the results obtained from the *a priori* tests, we performed *a posteriori* tests for various grid resolutions and Reynolds numbers. The anisotropy-resolving SGS model generally provided reasonable mean-velocity predictions even for high Reynolds numbers ($Re_\tau = 1000, 2000$) with coarse grid resolution ($\Delta x^+ = 100, \Delta z^+ = 50$). In contrast, the isotropic SGS model returned

considerable overpredictions in the mean-velocity distributions. The anisotropy-resolving SGS model showed a highly similar trend in the $\langle u''v'' \rangle$ budget near the wall for all *Re* cases. Although there remain some discrepancies to be further improved, this modeling concept is expected to work effectively in the near-wall region for higher *Re* practical LES.

Finally, we note the following as areas of future study. An important factor to be considered in this study is the filtering operator. We used a top-hat filter to decompose the variables into GS and SGS components. Generally, we understand that the SGS component consists mainly of the high-wavenumber modes. However, the SGS component obtained with the top-hat filter involves a significant effect from the low-wavenumber region, although it also covers most of the high-wavenumber region. This indicates that the statistical value of the SGS component may show a trend that derives from the low-wavenumber region. This may be why the SGS-stress anisotropy calculated using the top-hat filter is not isotropic but, rather, similar to that of the GS *Re* stress, as found in our previous studies.[17,26]

If we consider a wide range of engineering applications, we have to adopt strategies, such as a generalized coordinate system, unstructured grid system, or building-cube method, to deal with complex geometries. Under such difficult conditions, we cannot use the sharp cutoff filter based on the spectral method and have to adopt the top-hat or Gaussian filter, which can be directly applied to complex geometries. Therefore, we must always consider the effect of the low-wavenumber region in the SGS component. Regarding this topic, Piomelli *et al.*[24] suggested using a mixed SGS model combined with the Gaussian filter. Because the top-hat filter generally has a trend similar to the Gaussian filter, the information presently obtained generally corresponds to that found by Piomelli *et al.*[24]

Many mixed-type SGS models have been proposed so far. Although they show greater potential than conventional EVM-type SGS models, they have rarely been used in practical engineering applications. The main reason for this may be the computational instability in their application to turbulent flows with complex geometries. However, the effective strategy[16] proposed to overcome this difficulty makes it possible to use anisotropy-resolving SGS models practically. Improving LES performance for a wide range of grid resolutions with complex geometries requires further study on the effect of an SGS model on predicting the GS component. The budget of the resolved GS *Re* stress is thought to be particularly important.

ACKNOWLEDGMENTS

The present computation was primarily carried out using the computer facilities at the Research Institute for Information Technology, Kyushu University, Japan. This research was supported by JSPS KAKENHI Grant No. JP19K12005.

REFERENCES

[1]J. Smagorinsky, "General circulation experiments with the primitive equations: I. The basic experiment," Mon. Weather Rev. **91**, 99–164 (1963).
[2]M. Germano, U. Piomelli, P. Moin, and W. H. Cabot, "A dynamic subgrid-scale eddy viscosity model," Phys. Fluids A **3**, 1760–1765 (1991).
[3]D. K. Lilly, "A proposed modification of the Germano subgridscale closure method," Phys. Fluids A **4**, 633–635 (1992).
[4]S. T. Bose, P. Moin, and D. You, "Grid-independent large-eddy simulation using explicit filtering," Phys. Fluids **22**, 105103 (2010).
[5]S. Hickel, C. P. Egerer, and J. Larsson, "Subgrid-scale modeling for implicit large eddy simulation of compressible flows and shock-turbulence interactions," Phys. Fluids **26**, 106101 (2014).
[6]L. Guedot, G. Lartigue, and V. Moureau, "Design of implicit high-order filters on unstructured grids for the identification of large-scale features in large-eddy simulation and application to a swirl burner," Phys. Fluids **27**, 045107 (2015).
[7]F. Orley, T. Trummler, S. Hickel, M. S. Mihatsch, S. J. Schmidt, and N. A. Adams, "Large-eddy simulation of cavitating nozzle flow and primary jet break-up," Phys. Fluids **27**, 086101 (2015).
[8]J. Bardina, J. H. Ferziger, and W. C. Reynolds, "Improved subgrid scale models for large eddy simulation," AIAA Paper No. 80-1357, 1980.
[9]K. Horiuti, "A proper velocity scale for modeling subgrid-scale eddy viscosities in large eddy simulation," Phys. Fluids A **5**, 146–157 (1993).
[10]Y. Zang, R. L. Street, and J. R. Koseff, "A dynamic mixed subgrid-scale model and its application to turbulent recirculating flows," Phys. Fluids A **5**, 3186–3196 (1993).
[11]M. V. Salvetti and S. Banerjee, "*A priori* tests of a new dynamic subgridscale model for finite difference large eddy simulations," Phys. Fluids **7**, 2831–2847 (1995).
[12]B. Vreman, B. Geurts, and H. Kuerten, "On the formulation of the dynamic mixed subgrid-scale model," Phys. Fluids **6**, 4057–4059 (1994).
[13]K. Horiuti, "A new dynamic two-parameter mixed model for large-eddy simulation," Phys. Fluids **9**, 3443–3464 (1997).
[14]F. Sarghini, U. Piomelli, and E. Balaras, "Scale-similar models for large-eddy simulations," Phys. Fluids **11**, 1596–1607 (1999).
[15]Y. Morinishi and O. V. Vasilyev, "A recommended modification to the dynamic two-parameter mixed subgrid scale model for large eddy simulation of wall bounded turbulent flow," Phys. Fluids **13**, 3400–3410 (2001).
[16]K. Abe, "An improved anisotropy-resolving subgrid-scale model with the aid of a scale-similarity modeling concept," Int. J. Heat Fluid Flow **39**, 42–52 (2013).
[17]K. Abe, "An investigation of SGS-stress anisotropy modeling in complex turbulent flow fields," Flow, Turbul. Combust. **92**, 503–525 (2014).
[18]T. Ohtsuka and K. Abe, "On the role of an anisotropy-resolving extra term for a subgrid-scale model in near-wall turbulence," J. Comput. Sci. Technol. **7**, 410–425 (2013).
[19]K. Abe and T. Ohtsuka, "On the effect of an anisotropy-resolving subgrid-scale model on turbulent vortex motions," in Proceedings of the 10th International Symposium on Engineering Turbulence Modelling and Measurements, Marbella, Spain, 2014, Paper No. S4-1.
[20]K. Abe, "Investigation of the effect of an anisotropy-resolving subgrid-scale model on budgets of the Reynolds stresses," in Proceedings of the 11th International Symposium on Turbulence and Shear Flow Phenomena, Southampton, UK, 2019, Paper No. P-21.
[21]R. D. Moser, J. Kim, and N. N Mansour, "Direct numerical simulation of turbulent channel flow up to $Re_\tau = 590$," Phys. Fluids **11**, 943–945 (1999).
[22]M. Lee and R. D. Moser, "Direct numerical simulation of turbulent channel flow up to $Re_\tau = 5200$," J. Fluid Mech. **774**, 395–415 (2015).
[23]S. Toosi and J. Larsson, "Anisotropic grid-adaptation in large eddy simulations," Comput. Fluids **156**, 146–161 (2017).
[24]U. Piomelli, P. Moin, and J. H. Ferziger, "Model consistency in large eddy simulation of turbulent channel flows," Phys. Fluids **31**, 1884–1891 (1988).
[25]M. Inagaki, "A new wall-damping function for large eddy simulation employing Kolmogorov velocity scale," Int. J. Heat Fluid Flow **32**, 26–40 (2011).
[26]T. Ohtsuka and K. Abe, "Toward the development of an anisotropy-resolving subgrid-scale model for large eddy simulation," J. Fluid Sci. Technol. **9**, JFST0004 (2014).